Aalborg Universitet

On Channel Emulation Methods in Multiprobe Anechoic Chamber Setups for Over-The-Air Testing

Ji, Yilin; Fan, Wei; Pedersen, Gert F.; Wu, Xingfeng

On Channel Emulation Methods in Multi-Probe Anechoic Chamber Setups for Over-The-Air Testing

Yilin Ji, Wei Fan, Gert F. Pedersen, Xingfeng Wu

Abstract—Multiple-input multiple-output (MIMO) over-the-air (OTA) testing gives a way to evaluate the radio performance of MIMO-capable devices under realistic propagation channels as an alternative to expensive and uncontrollable drive testing. In this paper, we review two major channel emulation methods for MIMO OTA testing under the multi-probe anechoic chamber (MPAC) setup, i.e. the prefaded signals synthesis (PFS) and the plane wave synthesis (PWS). The target channel model for emulation is the geometry-based stochastic channel model (GSCM). The signal models for both channel emulation methods for the whole link from the transmitter (Tx) side to the receiver (Rx) side are given. The comparison analysis gives some new insights into the two channel emulation methods. The analytic expression of the joint space-time correlation function is derived for both methods in comparison to that of the target channel. It shows the cluster-wise channel emulated by the PFS method is Kronecker structured, which is different from the general definition of GSCMs. In contrast, the channel emulated with the PWS method is consistent with GSCMs. Moreover, the emulation accuracy for the two methods are compared under different target channel settings, i.e. different cluster angular spreads. The simulation results demonstrate the advantage of the PWS method over the PFS method, especially when cluster angular spreads are small.

Index Terms—MIMO OTA testing, MPAC, channel emulation methods, space-time correlation.

I. Introduction

Multiple-input multiple-output (MIMO) over-the-air (OTA) testing [1] currently plays an important role in evaluating the radio performance of any MIMO-capable device in different development stages, e.g. early-stage prototyping and mid-term refinement, before final massive roll-out. It helps researchers to reveal the potential flaws and non-idealities of the products during the design and manufacturing phase. The conventional way to conduct MIMO performance testing is called MIMO conducted testing. In conducted testing, the shell of the device-under-test (DUT) needs to be opened, and antenna ports on the DUT need to be reserved for cable connection. However, OTA testing does not suffer from these limitations. Therefore, it is standardized that the radiated performance testing of MIMO-capable devices must be performed over-the-air [1].

Yilin Ji, Wei Fan, and Gert F. Pedersen are with the Antenna Propagation and Millimeter-wave Systems (APMS) section at the Department of Electronic Systems, Falculty of Engineering and Science, Aalborg University, Denmark. Email: {yilin, wfa, gfp}@es.aau.dk. (Corresponding author: Wei Fan.)

Xingfeng Wu is with the Hardware Test Department, Huawei Device Co., Ltd., Beijing. Email: benny.wuxingfeng@huawei.com

In general, the implementation of MIMO OTA testing can be divided into three main categories, i.e. the radiated two-stage (RTS) methods [2], [3], the reverberation chamber (RC) based methods [4], [5], and the multi-probe anechoic chamber (MPAC) based methods [6]–[9]. The RTS method evolves from the conducted two-stage method [10] where the physical cable connection between the channel emulator (CE) output ports and the DUT antenna ports is approached over-the-air in an anechoic chamber. By introducing a so-called calibration matrix in the CE, the product of the calibration matrix and the transfer matrix between the CE output ports and the DUT antenna ports yields (or approximates) an identity matrix. In other words, the signals received at the DUT antenna ports are approximately the same as from the conducted two-stage method as if cables were used. Therefore, this method is also called wireless cable method [3]. Due to the use of CEs, arbitrary channel models can be implemented with the RTS method. However, the antenna array field pattern needs to be measured in the first stage with the internal receivers of the DUT and synthesized in the CE in the second stage, which means the DUT antenna response is not inherently included during the testing. Hence, the RTS method is not suitable for DUTs with reconfigurable or adaptive antenna patterns [3]. The second category is the RC based method, which generates isotropic spatial channels with Rayleigh fading by rotating mechanical stirrers and DUT in the reverberation chamber (metallic cavity). Unlike the RTS method, the DUT antenna pattern is directly included in the testing. However, the drawback of the RC based method is its limited control on the reproduced channels. The third category is the MPAC based method, which is standardized in CTIA [11] for its capability of reproducing standard channel models, i.e. geometry-based stochastic channel models (GSCMs), such as 3GPP SCM [12], SCME [13], and WINNER II model [14].

Two channel emulation methods, which are shown later in the paper, are usually adopted with MPAC setups, namely the prefaded signals synthesis (PFS) [7], [15], and the plane wave synthesis (PWS) [6]–[9]. The verification of both methods is usually done with channel characteristics in different domains, e.g. spatial correlation function (SCF) on the transmitter (Tx) side, SCF on the receiver (Rx) side, temporal correlation function (TCF), power delay profile, and cross-polarization ratio (XPR) [7], [16]. However, the verification in joint domain, e.g. the SCF in joint Tx-Rx space domain, is rarely mentioned. Moreover, the PFS and the PWS method are usually considered to be equally capable of emulating GSCMs [7], [17]. In this paper, the signal models for the emulated channels with the PFS and the PWS method are given. The space-time corre-
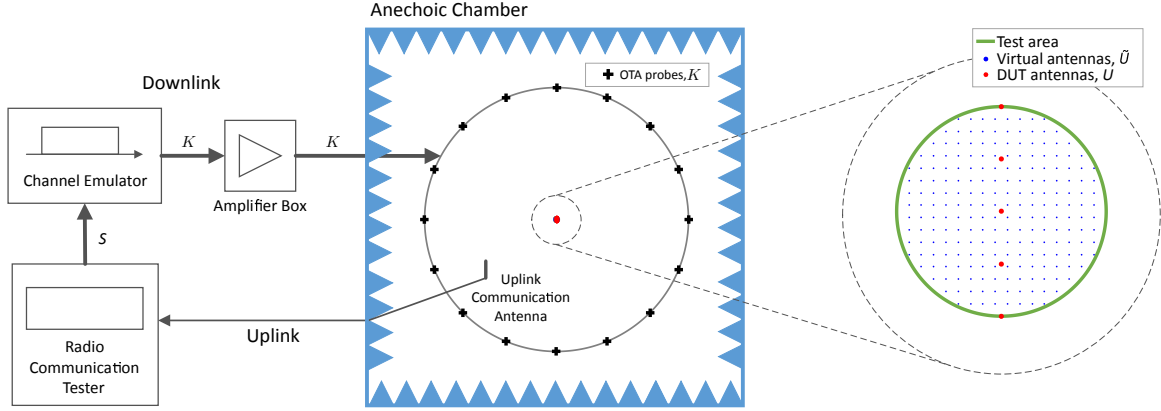
Fig. 1. The diagram of MIMO OTA testing with an MPAC setup [16]. Note the DUT antennas are illustrated as a ULA, but they can be of arbitrary structures in practice.

lation function (STCF) [18]–[21] is derived for both methods in joint Tx space, Rx space, and time domain. Comparisons are made to the STCF of the target channel model for the first time in the literature. The commonly-believed equivalence in emulation accuracy for the two methods is evaluated. The simulation in SCF on the Rx side shows that this is only valid when the cluster angular spread of the target channel is large.

The contribution of this paper lies in the following aspects:

- The signal models of the emulated channels for the whole link from the Tx side to the Rx side are given for both the PFS and the PWS method.
- The STCF in the joint domain, i.e. the spatial domain on the Tx side, the spatial domain on the Rx side, and the time domain, is derived for both methods, which reveals the Kronecker structure of the cluster-wise emulated channel with the PFS method. This feature is important, yet not known for the PFS method.
- The emulation accuracy of the two methods is compared in terms of the SCF of the emulated channels on the Rx side under different target channel settings, i.e. cluster angular spreads. It is demonstrated that the commonly-believed equivalence in channel emulation capabilities is only valid when the cluster spread is large.

The rest of the paper is organized as follows: In Section II, the principles of the PFS and the PWS method are reviewed. In Section III, the STCF of the emulated channel is derived for both methods, and the difference to that of the target channel is discussed. In Section IV, the emulation accuracy of the two methods are compared under different target channel settings. Section V concludes the paper.

The notation used in this paper is as follows: $(\cdot)^{\mathrm{T}}$ denotes the transpose operator, $(\cdot)^*$ the complex conjugate operator, $\|\cdot\|$ the Euclidean norm, $\langle\cdot,\cdot\rangle$ the inner product operator, and $\mathrm{E}\{\cdot\}$ the expectation operator.

II. PRINCIPLE OF CHANNEL EMULATION METHODS UNDER MPAC SETUP

The diagram of MIMO OTA testing with the MPAC setup is shown in Fig. 1. The whole system consists of a radio communication tester, a CE, a power amplifier box, and a number of OTA probes located inside an anechoic chamber. For the downlink, test signals are generated from a radio communication tester, which mimics the behaviour of a Tx equipped with S antennas. The test signals are transmitted to the CE via cables, and further convolved with the channel in the CE, which is generated according to the standard channel models. The output signals from the CE are fed to K OTA probes inside the anechoic chamber after being power amplified. The target spatial profiles on the Rx side, i.e. the DUT side, are generated in the so-called test area over-the-air with the channel emulation methods. The DUT with U antennas is placed in the test area to perform the testing. Note the DUT antennas are illustrated as a uniform linear array (ULA) in Fig. 1, but they can be of arbitrary structures in practice. The focus of the testing is on the downlink, and usually only one communication antenna is placed in the anechoic chamber for uplink communication.

The goal of the channel emulation methods is to reproduce the spatial profiles of the target channel on the Rx side in the test area with the MPAC setup. The PFS method and the PWS method achieve the objective in two different ways. In this section, we introduce the target channel models, i.e. the GSCMs, and the two channel emulation methods, i.e. the PFS and the PWS method.

A. Target Channel Models

For a MIMO system with S antenna elements on the Tx array and U antenna elements on the Rx array, the time-variant channel transfer function $h_{u,s}(t,f)$ between the sth Tx element and the uth Rx element can be expressed as [12]

$$h_{u,s}(t,f) = \sum_{n=1}^{N} h_{u,s,n}(t,f), \qquad (1)$$

This article has been accepted for publication in a future issue of this journal, but has not been fully edited. Content may change prior to final publication. Citation information: DOI 10.1109/TVT.2018.2824403, IEEE Transactions on Vehicular Technology

3

where N is the number of clusters, t denotes the time, and f the frequency. The contribution of the nth cluster can be further expressed as

$$
\begin{aligned}
&h_{u,s,n}(t,f)\\
&= \sqrt{\frac{P_n}{M}} \sum_{m=1}^{M} \begin{bmatrix} F_{s,\text{Tx}}^{V}(\varphi_{n,m}) \\ F_{s,\text{Tx}}^{H}(\varphi_{n,m}) \end{bmatrix}^{\text{T}} \mathbf{A} \begin{bmatrix} F_{u,\text{Rx}}^{V}(\phi_{n,m}) \\ F_{u,\text{Rx}}^{H}(\phi_{n,m}) \end{bmatrix}\\
&\quad \cdot \exp(j2\pi\vartheta_{n,m}t)\exp(-j2\pi f\tau_n),
\end{aligned} \tag{2}
$$

where P_n and τ_n are the power and the delay of the nth cluster, respectively. M is the number of subpaths for each cluster, $F_{s,\text{Tx}}^{V}$ and $F_{s,\text{Tx}}^{H}$ are the antenna field patterns of the sth Tx antenna for vertical and horizontal polarization, respectively. Similarly, $F_{u,\text{Rx}}^{V}$ and $F_{u,\text{Rx}}^{H}$ are the antenna field patterns of the uth Rx antenna for vertical and horizontal polarization, respectively. $\varphi_{n,m}$, $\phi_{n,m}$, and $\vartheta_{n,m}$ are the angle of departure (AoD), angle of arrival (AoA), and Doppler frequency of the mth subpath of the nth cluster, respectively. Note that the antenna field pattern is defined with a common phase center over the antenna array, so the phase differences corresponding to the array geometry are inherently included. $\mathbf{A}$ is the polarization matrix, and can be written as

$$
\mathbf{A} = \begin{bmatrix} \exp\left(j\Phi_{n,m}^{VV}\right) & \sqrt{\kappa_{n,m}}\exp\left(j\Phi_{n,m}^{VH}\right) \\ \sqrt{\kappa_{n,m}}\exp\left(j\Phi_{n,m}^{HV}\right) & \exp\left(j\Phi_{n,m}^{HH}\right) \end{bmatrix} \tag{3}
$$

where $\Phi_{n,m}^{VV}$, $\Phi_{n,m}^{VH}$, $\Phi_{n,m}^{HV}$, and $\Phi_{n,m}^{HH}$ are independent and identically distributed (i.i.d.) random variables which are uniformly distributed over $[0, 2\pi]$. $\kappa_{n,m}$ is the XPR of the mth subpath of the nth cluster.

For MPAC based methods, the key problem to solve is to reproduce the target spatial profile on the Rx side over-the-air, since the other channel properties, e.g. spatial profile on the Tx side, Doppler spectrum, power delay profile, and XPR, can be perfectly reproduced in the CE [16], [22]. The dual polarization control is realized by using OTA probes with two co-located orthogonally polarized elements with independent feeds. For simplicity, we only discuss the vertical polarization case hereafter. In the single polarization case, the polarization matrix $\mathbf{A}$ diminishes to a scalar, and (2) is simplified to

$$
\begin{aligned}
&h_{u,s,n}(t,f)\\
&= \sqrt{\frac{P_n}{M}} \sum_{m=1}^{M} F_s^{\text{Tx}}(\varphi_{n,m}) F_u^{\text{Rx}}(\phi_{n,m})\\
&\quad \cdot \exp(j2\pi\vartheta_{n,m}t + j\Phi_{n,m}) \cdot \exp(-j2\pi f\tau_n),
\end{aligned} \tag{4}
$$

where F_s^{Tx} and F_u^{Rx} are the vertically polarized antenna field pattern for the sth Tx antenna and uth Rx antenna, respectively. $\Phi_{n,m}$ is the i.i.d. random initial phase of the mth subpath of the nth cluster. We further restrict our discussion to two-dimensional (2D) channel models, which means the OTA probes and the test area are in the same plane, i.e. the azimuth plane. Consequently, AoDs and AoAs correspond to azimuth angles.

B. Prefaded Signals Synthesis Method

For link level simulations, channels are generated based on drops, within which channel parameters are fixed and

motions are only virtual [14]. Due to the wide-sense stationary uncorrelated scattering (WSSUS) assumption [18]–[20] for every drop, the channel can be fully characterized with its second-order statistics, i.e. the correlation functions. The PFS method generates the channel, whose correlation functions approximate those of the target channel cluster-wise.

For an MPAC setup equipped with K OTA probes, the transfer function emulated with the PFS method from the sth Tx antenna to the kth OTA probe for the nth cluster can be expressed as

$$
\begin{aligned}
&\hat{h}_{k,s,n}^{\text{PFS}}(t,f)\\
&= \sqrt{\frac{P_n}{M}} \sum_{m=1}^{M} F_s^{\text{Tx}}(\varphi_{n,m}) \sqrt{g_{n,k}}\\
&\quad \cdot \exp(j2\pi\vartheta_{n,m}t + j\Phi_{n,m,k}) \cdot \exp(-j2\pi f\tau_n),
\end{aligned} \tag{5}
$$

where $\Phi_{n,m,k}$ is the i.i.d. random initial phase of the mth subpath of the nth cluster for the kth OTA probe. $g_{n,k}$ is the power weight applied on the kth OTA probe for the nth cluster with $\sum_{k=1}^{K} g_{n,k} = 1$.

In order to observe the emulated channel in the test area, the test area is sampled with $\tilde{U}$ virtual isotropic antennas. The emulated channel observed at the $\tilde{u}$th virtual antenna (VA) from the sth Tx antenna for the nth cluster can be calculated as the sum of the contribution from all K OTA probes as

$$
\begin{aligned}
&\hat{h}_{\tilde{u},s,n}^{\text{PFS}}(t,f)\\
&= \sum_{k=1}^{K} \hat{h}_{k,s,n}^{\text{PFS}}(t,f) \cdot F_{\tilde{u}}^{\text{VA}}(\phi_k^{\text{OTA}})\\
&= \sqrt{\frac{P_n}{M}} \sum_{k=1}^{K} \sum_{m=1}^{M} F_s^{\text{Tx}}(\varphi_{n,m}) F_{\tilde{u}}^{\text{VA}}(\phi_k^{\text{OTA}}) \sqrt{g_{n,k}}\\
&\quad \cdot \exp(j2\pi\vartheta_{n,m}t + j\Phi_{n,m,k}) \cdot \exp(-j2\pi f\tau_n),
\end{aligned} \tag{6}
$$

where $F_{\tilde{u}}^{\text{VA}}(\phi_k^{\text{OTA}})$ is the antenna field pattern of the virtual antenna $\tilde{u}$ with $\|F_{\tilde{u}}^{\text{VA}}\| = 1$. $\phi_k^{\text{OTA}} = 2\pi(k-1)/K$ is the angle where the kth OTA probe is located with respect to the center of the test area. Note that the antenna patterns of the OTA probes and the power loss due to the free-space propagation from the OTA probes to the test area are omitted in (6) because the transmitting power of each OTA probe is calibrated to the same level with a calibration antenna in the center of the test area. Moreover, since the OTA probes are placed in the far field of the test area, the plane wave assumption holds across the test area with respect to each OTA probe. Also, the power variation within the test area from each OTA probe is negligible.

The spatial profile of each cluster of the target channel on the Rx side is emulated by assigning a proper power weight $g_{n,k}$ to the kth OTA probe for the nth cluster so that the emulated spatial profile in the test area approaches the target one. The spatial correlation of the nth cluster of the target channel for an arbitrary virtual antenna pair $(\tilde{u}_1, \tilde{u}_2)$ with $\tilde{u}_1 \in$

$[1, \tilde{U}]$ and $\tilde{u}_2 \in [1, \tilde{U}]$ can be calculated as

$$
\rho_{\tilde{u}_1, \tilde{u}_2} = \frac{1}{\beta_0} \cdot \mathrm{E} \left\{ h_{\tilde{u}_1, s, n}(t, f) \cdot h_{\tilde{u}_2, s, n}(t, f)^* \right\}
$$
$$
= \frac{1}{M} \sum_{m=1}^{M} F_{\tilde{u}_1}^{\mathrm{VA}}(\phi_{n,m}) F_{\tilde{u}_2}^{\mathrm{VA}}(\phi_{n,m})^*, \qquad (7)
$$

where $h_{\tilde{u}, s, n}(t, f)$ is calculated from (4) with the virtual antenna $\tilde{u}$ as the Rx antenna. $\beta_0 = P_n$ is the normalization factor to force $\rho_{\tilde{u}_1, \tilde{u}_2} = 1$ when $\tilde{u}_1 = \tilde{u}_2$. The detailed derivation for (7) is given in Appendix A. The corresponding spatial correlation of the emulated channel can be derived similarly as for the target channel as

$$
\hat{\rho}_{\tilde{u}_1, \tilde{u}_2} = \frac{1}{\hat{\beta}_0} \cdot \mathrm{E} \left\{ \hat{h}_{\tilde{u}_1, s, n}^{\mathrm{PFS}}(t, f) \cdot \hat{h}_{\tilde{u}_2, s, n}^{\mathrm{PFS}}(t, f)^* \right\}
$$
$$
= \sum_{k=1}^{K} g_{n,k} F_{\tilde{u}_1}^{\mathrm{VA}}(\phi_k^{\mathrm{OTA}}) F_{\tilde{u}_2}^{\mathrm{VA}}(\phi_k^{\mathrm{OTA}})^*, \qquad (8)
$$

where $\hat{\beta}_0 = P_n$ is the normalization factor to force $\hat{\rho}_{\tilde{u}_1, \tilde{u}_2} = 1$ when $\tilde{u}_1 = \tilde{u}_2$. The detailed derivation for (8) is given in Appendix B.

The power weight vector $\boldsymbol{g}_n = [g_{n,1}, ..., g_{n,K}]$ is obtained by solving the optimization problem

$$
\underset{\boldsymbol{g}_n}{\arg \min} \| \rho_{\tilde{u}_1, \tilde{u}_2} - \hat{\rho}_{\tilde{u}_1, \tilde{u}_2}(\boldsymbol{g}_n) \|^2, \qquad (9)
$$

for all combinations of $(\tilde{u}_1, \tilde{u}_2)$ pairs. Equation (9) is convex and can be solved efficiently [23]. Finally, the emulated channel for the nth cluster from the sth Tx antenna to the uth DUT antenna can be written as

$$
\hat{h}_{u, s, n}^{\mathrm{PFS}}(t, f)
$$
$$
= \sqrt{\frac{P_n}{M}} \sum_{k=1}^{K} \sum_{m=1}^{M} F_s^{\mathrm{Tx}}(\varphi_{n,m}) F_u^{\mathrm{Rx}}(\phi_k^{\mathrm{OTA}}) \sqrt{g_{n,k}}
$$
$$
\cdot \exp(j2\pi \vartheta_{n,m} t + j\Phi_{n,m,k}) \cdot \exp(-j2\pi f \tau_n). \qquad (10)
$$

C. Plane Wave Synthesis Method

In comparison to the PFS method, where the target channel model is emulated cluster-wise, the PWS method is capable of reproducing each subpath within clusters. For the PWS method, the channel transfer function from the sth Tx antenna to the kth OTA probe for the mth subpath of the nth cluster can be written as [7]

$$
\hat{h}_{k, s, n, m}^{\mathrm{PWS}}(t, f)
$$
$$
= \sqrt{\frac{P_n}{M}} F_s^{\mathrm{Tx}}(\varphi_{n,m}) \cdot w_{n,m,k}
$$
$$
\cdot \exp(j2\pi \vartheta_{n,m} t + j\Phi_{n,m}) \cdot \exp(-j2\pi f \tau_n), \qquad (11)
$$

where $w_{n,m,k}$ is the complex weight added on the kth OTA probe for the mth subpath of the nth cluster. Note that unlike the PFS method where real-valued power weights are applied, complex-valued weights are used in the PWS method. Again, virtual antennas are introduced in the test area to observe the emulated channel. The emulated channel observed on

the virtual antenna $\tilde{u}$ can be calculated as the sum of the contribution from all K OTA probes as

$$
\hat{h}_{\tilde{u}, s, n, m}^{\mathrm{PWS}}(t, f)
$$
$$
= \sum_{k=1}^{K} \hat{h}_{k, s, n, m}^{\mathrm{PWS}}(t, f) \cdot F_{\tilde{u}}^{\mathrm{VA}}(\phi_k^{\mathrm{OTA}})
$$
$$
= \sqrt{\frac{P_n}{M}} \sum_{k=1}^{K} F_s^{\mathrm{Tx}}(\varphi_{n,m}) F_{\tilde{u}}^{\mathrm{VA}}(\phi_k^{\mathrm{OTA}}) \cdot w_{n,m,k}
$$
$$
\cdot \exp(j2\pi \vartheta_{n,m} t + j\Phi_{n,m}) \cdot \exp(-j2\pi f \tau_n). \qquad (12)
$$

Since the array response of a single plane wave from the target AoA $\phi_{n,m}$ on the $\tilde{u}$th virtual antenna is $F_{\tilde{u}}^{\mathrm{VA}}(\phi_{n,m})$, the complex weight vector $\boldsymbol{w}_{n,m} = [w_{n,m,1}, ..., w_{n,m,K}]$ is calculated by

$$
\underset{\boldsymbol{w}_{n,m}}{\arg \min} \sum_{\tilde{u}=1}^{\tilde{U}} \left\| \sum_{k=1}^{K} F_{\tilde{u}}^{\mathrm{VA}}(\phi_k^{\mathrm{OTA}}) \cdot w_{n,m,k} - F_{\tilde{u}}^{\mathrm{VA}}(\phi_{n,m}) \right\|^2.
$$
$$
(13)
$$

Equation (13) can be solved with the least squares method. Finally, the emulated channel for the mth subpath of the nth cluster from the sth Tx antenna to the uth DUT antenna with the PWS method results in

$$
\hat{h}_{u, s, n, m}^{\mathrm{PWS}}(t, f)
$$
$$
= \sqrt{\frac{P_n}{M}} \sum_{k=1}^{K} F_s^{\mathrm{Tx}}(\varphi_{n,m}) F_u^{\mathrm{Rx}}(\phi_k^{\mathrm{OTA}}) \cdot w_{n,m,k}
$$
$$
\cdot \exp(j2\pi \vartheta_{n,m} t + j\Phi_{n,m}) \cdot \exp(-j2\pi f \tau_n). \qquad (14)
$$

Using channel linearity, we can further obtain the contribution of the nth cluster of the emulated channel from the sth Tx antenna to the uth DUT antenna with the PWS method as

$$
\hat{h}_{u, s, n}^{\mathrm{PWS}}(t, f)
$$
$$
= \sqrt{\frac{P_n}{M}} \sum_{m=1}^{M} \sum_{k=1}^{K} F_s^{\mathrm{Tx}}(\varphi_{n,m}) F_u^{\mathrm{Rx}}(\phi_k^{\mathrm{OTA}}) \cdot w_{n,m,k}
$$
$$
\cdot \exp(j2\pi \vartheta_{n,m} t + j\Phi_{n,m}) \cdot \exp(-j2\pi f \tau_n). \qquad (15)
$$

Note that since the PWS method utilizes complex weights on OTA probes for each subpath, both power and phase calibration are needed before testing, which is more demanding than the PFS method in terms of calibration complexity. It was shown in [24] that both power and phase calibration can be achieved at high accuracy for traditional user equipment (UE) OTA testing. However, for the upcoming fifth-generation (5G) communication systems [25]–[28], the phase calibration could be difficult to achieve for base station (BS) OTA testing due to the non-linearity of radio frequency (RF) components, e.g. switches and power amplifiers, at high frequency band, and the increased number of OTA probes. Nonetheless, the hardware resources required for the PFS and the PWS method are identical for testing the same DUT.

III. SPACE-TIME CORRELATION FUNCTION ANALYSIS

In this section, we derive the cluster-wise STCF of the emulated channels for the PFS and the PWS method in comparison

to that of the target channel model. It is straightforward to extend the derived cluster-wise STCF for the whole channel with multiple clusters due to channel linearity. In order to focus on the channel properties, both the Tx and the Rx antennas are assumed to be isotropic, i.e. $\|F_s^{\mathrm{Tx}}\| = \|F_u^{\mathrm{Rx}}\| = 1$. We further assume the target channel can be perfectly emulated by the PFS and the PWS method in the test area. There exists a power weight vector $\boldsymbol{g}_n$ with $n \in [1, N]$ for the PFS method that yields

$$\hat{\rho}_{u_1,u_2} = \rho_{u_1,u_2}, \tag{16}$$

for all (u_1, u_2) DUT antenna pairs with $u_1 \in [1, U]$ and $u_2 \in [1, U]$. Similarly, there exists a complex weight vector $\boldsymbol{w}_{n,m}$ with $n \in [1, N]$ and $m \in [1, M]$ for the PWS method that yields

$$\sum_{k=1}^{K} F_u^{\mathrm{Rx}}(\phi_k^{\mathrm{OTA}}) \cdot w_{n,m,k} = F_u^{\mathrm{Rx}}(\phi_{n,m}), \tag{17}$$

for all U DUT antennas. This assumption can be approximately achieved when the number of OTA probes is sufficient to support the desired test area size with respect to an acceptable emulation error, e.g. within 0.2 in deviation from the target SCF [7].

A. The STCF for the Target Channel Model

Using the property of the i.i.d. random initial phase $\Phi_{n,m}$ in (4), the STCF for the nth cluster of the target channel can be derived as

$$
\begin{aligned}
&R(u_1, s_1, t_1; u_2, s_2, t_2) \\
&= \frac{1}{\beta_0} \cdot \mathrm{E}\{h_{u_1,s_1,n}(t_1, f) \cdot h_{u_2,s_2,n}(t_2, f)^*\} \\
&= \frac{1}{M} \sum_{m=1}^{M} F_{s_1}^{\mathrm{Tx}}(\varphi_{n,m}) F_{s_2}^{\mathrm{Tx}}(\varphi_{n,m})^* F_{u_1}^{\mathrm{Rx}}(\phi_{n,m}) \\
&\quad \cdot F_{u_2}^{\mathrm{Rx}}(\phi_{n,m})^* \exp(j2\pi\vartheta_{n,m}t_1) \exp(j2\pi\vartheta_{n,m}t_2)^*, \tag{18}
\end{aligned}
$$

where $\beta_0 = P_n$ is the normalization factor to force $R(u_1, s_1, t_1; u_2, s_2, t_2) = 1$ when $u_1 = u_2$, $s_1 = s_2$, and $t_1 = t_2$. The derivation for (18) is similar to that given in Appendix A, and thus omitted here.

By assigning $u_1 = u_2$ and $t_1 = t_2$, we obtain the target SCF on the Tx side,

$$R(s_1; s_2) = \frac{1}{M} \sum_{m=1}^{M} F_{s_1}^{\mathrm{Tx}}(\varphi_{n,m}) F_{s_2}^{\mathrm{Tx}}(\varphi_{n,m})^*. \tag{19}$$

By assigning $s_1 = s_2$ and $t_1 = t_2$, we obtain the target SCF on the Rx side,

$$R(u_1; u_2) = \frac{1}{M} \sum_{m=1}^{M} F_{u_1}^{\mathrm{Rx}}(\phi_{n,m}) F_{u_2}^{\mathrm{Rx}}(\phi_{n,m})^*. \tag{20}$$

By assigning $s_1 = s_2$ and $u_1 = u_2$, we obtain the target TCF,

$$R(t_1; t_2) = \frac{1}{M} \sum_{m=1}^{M} \exp(j2\pi\vartheta_{n,m}t_1) \exp(j2\pi\vartheta_{n,m}t_2)^*. \tag{21}$$

B. The STCF for the PFS Method

Using the property of the i.i.d. random initial phase $\Phi_{n,m,k}$ in (10), the STCF for the nth cluster of the emulated channel with the PFS method can be derived as

$$
\begin{aligned}
&\hat{R}^{\mathrm{PFS}}(u_1, s_1, t_1; u_2, s_2, t_2) \\
&= \frac{1}{\hat{\beta}_0^{\mathrm{PFS}}} \cdot \mathrm{E}\left\{\hat{h}_{u_1,s_1,n}^{\mathrm{PFS}}(t_1, f) \cdot \hat{h}_{u_2,s_2,n}^{\mathrm{PFS}}(t_2, f)^*\right\} \\
&= \frac{1}{M} \sum_{m=1}^{M} F_{s_1}^{\mathrm{Tx}}(\varphi_{n,m}) F_{s_2}^{\mathrm{Tx}}(\varphi_{n,m})^* \exp(j2\pi\vartheta_{n,m}t_1) \\
&\quad \cdot \exp(j2\pi\vartheta_{n,m}t_2)^* \cdot \sum_{k=1}^{K} g_{n,k} F_{u_1}^{\mathrm{Rx}}(\phi_k^{\mathrm{OTA}}) F_{u_2}^{\mathrm{Rx}}(\phi_k^{\mathrm{OTA}})^*, \tag{22}
\end{aligned}
$$

where $\hat{\beta}_0^{\mathrm{PFS}} = P_n$ is the normalization factor. The derivation for (22) is similar to that given in Appendix B, and therefore omitted here. Using the equality in (16), (22) is recast to

$$
\begin{aligned}
&\hat{R}^{\mathrm{PFS}}(u_1, s_1, t_1; u_2, s_2, t_2) \\
&= \frac{1}{M^2} \sum_{m=1}^{M} F_{s_1}^{\mathrm{Tx}}(\varphi_{n,m}) F_{s_2}^{\mathrm{Tx}}(\varphi_{n,m})^* \exp(j2\pi\vartheta_{n,m}t_1) \\
&\quad \cdot \exp(j2\pi\vartheta_{n,m}t_2)^* \cdot \sum_{m'=1}^{M} F_{u_1}^{\mathrm{Rx}}(\phi_{n,m'}) F_{u_2}^{\mathrm{Rx}}(\phi_{n,m'})^*. \tag{23}
\end{aligned}
$$

By assigning $u_1 = u_2$ and $t_1 = t_2$, we obtain the emulated SCF on the Tx side,

$$\hat{R}^{\mathrm{PFS}}(s_1; s_2) = \frac{1}{M} \sum_{m=1}^{M} F_{s_1}^{\mathrm{Tx}}(\varphi_{n,m}) F_{s_2}^{\mathrm{Tx}}(\varphi_{n,m})^*. \tag{24}$$

By assigning $s_1 = s_2$ and $t_1 = t_2$, we obtain the emulated SCF on the Rx side,

$$\hat{R}^{\mathrm{PFS}}(u_1; u_2) = \frac{1}{M} \sum_{m=1}^{M} F_{u_1}^{\mathrm{Rx}}(\phi_{n,m}) F_{u_2}^{\mathrm{Rx}}(\phi_{n,m})^*. \tag{25}$$

By assigning $s_1 = s_2$ and $u_1 = u_2$, we obtain the emulated TCF,

$$\hat{R}^{\mathrm{PFS}}(t_1; t_2) = \frac{1}{M} \sum_{m=1}^{M} \exp(j2\pi\vartheta_{n,m}t_1) \exp(j2\pi\vartheta_{n,m}t_2)^*. \tag{26}$$

By comparing the SCF and TCF for the target channel, i.e. (19) to (21), with those for the emulated channel with the PFS method, i.e. (24) to (26), it can be seen the channel second-order characteristics are very well reproduced in each domain separately. However, in the joint domain, the target STCF in (18) is different from the emulated STCF in (23). Actually, it can be observed the emulated STCF has the Kronecker structure [29] between the joint AoD-Doppler domain and the AoA domain, i.e.

$$\hat{R}^{\mathrm{PFS}}(u_1, s_1, t_1; u_2, s_2, t_2) = \hat{R}^{\mathrm{PFS}}(s_1, t_1; s_2, t_2) \cdot \hat{R}^{\mathrm{PFS}}(u_1; u_2), \tag{27}$$

where $\hat{R}(s_1, t_1; s_2, t_2)$ is obtained by setting $u_1 = u_2$ in (23). Since the correlation function and the power spectrum are

This article has been accepted for publication in a future issue of this journal, but has not been fully edited. Content may change prior to final publication. Citation information: DOI 10.1109/TVT.2018.2824403, IEEE Transactions on Vehicular Technology

6

Fourier transform pairs in their respective domains [20], the Kronecker structure of the STCF indicates that the power AoD-Doppler spectrum is independent to the power AoA spectrum cluster-wise for the channel emulated with the PFS method. More intuitively, the same power AoD-Doppler spectrum would be seen by the DUT irrespective of the AoA within each cluster. Note this property is different from the general definition of the target channel model except the target channel model is set so specifically.

C. The STCF for the PWS Method

Using the property of the i.i.d. random initial phase $\Phi_{n,m}$ in (15), the STCF for the nth cluster of the emulated channel with the PWS method can be derived as

$$
\begin{aligned}
&\hat{R}^{\mathrm{PWS}}(u_1, s_1, t_1; u_2, s_2, t_2) \\
&= \frac{1}{\hat{\beta}_0^{\mathrm{PWS}}} \cdot \mathrm{E}\left\{ \hat{h}_{u_1,s_1,n}^{\mathrm{PWS}}(t_1, f) \cdot \hat{h}_{u_2,s_2,n}^{\mathrm{PWS}}(t_2, f)^* \right\} \\
&= \frac{1}{\hat{\beta}_0^{\mathrm{PWS}}} \frac{P_n}{M} \cdot \sum_{m=1}^{M} F_{s_1}^{\mathrm{Tx}}(\varphi_{n,m}) F_{s_2}^{\mathrm{Tx}}(\varphi_{n,m})^* \\
&\quad \cdot \exp(j2\pi\vartheta_{n,m}t_1) \exp(j2\pi\vartheta_{n,m}t_2)^* \\
&\quad \cdot \sum_{k=1}^{K} F_{u_1}^{\mathrm{Rx}}(\phi_k^{\mathrm{OTA}}) w_{n,m,k} \sum_{k'=1}^{K} F_{u_2}^{\mathrm{Rx}}(\phi_{k'}^{\mathrm{OTA}})^* w_{n,m,k'}^*, \quad (28)
\end{aligned}
$$

where

$$
\begin{aligned}
\hat{\beta}_0^{\mathrm{PWS}} = \frac{P_n}{M} &\sqrt{\sum_{m=1}^{M} \left\| \sum_{k=1}^{K} F_{u_1}^{\mathrm{Rx}}(\phi_k^{\mathrm{OTA}}) w_{n,m,k} \right\|^2} \\
&\cdot \sqrt{\sum_{m'=1}^{M} \left\| \sum_{k'=1}^{K} F_{u_2}^{\mathrm{Rx}}(\phi_{k'}^{\mathrm{OTA}}) w_{n,m',k'} \right\|^2}, \quad (29)
\end{aligned}
$$

is the normalization factor. Using the equality in (17), we can obtain

$$
\hat{R}^{\mathrm{PWS}}(u_1, s_1, t_1; u_2, s_2, t_2) = R(u_1, s_1, t_1; u_2, s_2, t_2). \quad (30)
$$

Straightforwardly, the respective correlation functions in individual domains, i.e. the SCF on the Tx/Rx side and the TCF, for the PWS method is the same as that of the target channel as well, and thus omitted here to avoid redundancy.

IV. EMULATION ACCURACY COMPARISON

As mentioned in Section II, reproducing the spatial profile on the Rx side is the goal for the MPAC based methods, since the other channel properties can be realized in the CE as in conducted testing. In this section, we first show the emulation accuracy of the PWS method in terms of relative field error (RFE). Then, we compare the emulated SCF on the Rx side between the PFS and the PWS method. The power spectrum in the joint AoD-AoA domain is lastly given to show the Kronecker structure of the emulated channel with the PFS method.

An MPAC setup with $K = 16$ OTA probes evenly located on the OTA ring is used for the simulation throughout this section, as shown in Fig. 2. The test area is set to $1.6\,\lambda$ in diameter, where λ denotes the wavelength at carrier frequency.
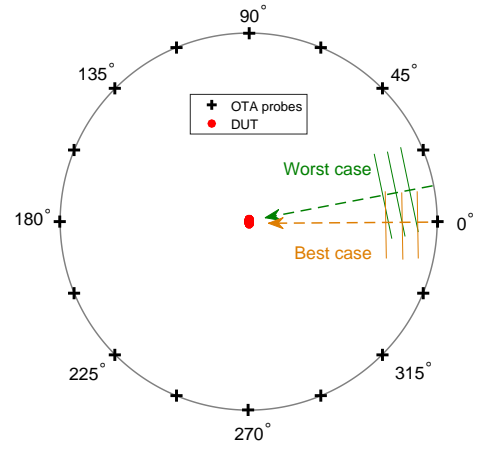

Fig. 2. The OTA probe configuration for the simulation in Section IV. "Best case" denotes the impinging angle at $0°$, and "Worst case" the impinging angle at $11.25°$.

A. RFE for the PWS Method

The target channel is set to a single plane wave with AoA ϕ_0. It is natural to see the target plane wave being well emulated when its AoA is aligned to any OTA probe, so we present two cases here to check the emulation accuracy of the PWS method, namely the best case and the worst case, as shown in Fig. 2. In the best case, ϕ_0 is set to $0°$ at which angle there locates an OTA probe. In the worst case, ϕ_0 is set to $11.25°$ which is the direction in the middle of two adjacent OTA probes.

The target and the emulated field are evaluated in the local area of size $2.4\,\lambda \times 2.4\,\lambda$ containing the test area. For any arbitrary location q in this local area, the amplitude of the target field can be expressed as

$$
F_q(\phi_0) = \exp\left(j\frac{2\pi}{\lambda}\langle \boldsymbol{r}_q, \boldsymbol{e}(\phi_0) \rangle \right) \quad (31)
$$

where $\boldsymbol{r}_q$ is the vector of coordinates for location q. $\boldsymbol{e}(\phi_0)$ is the unit vector pointing at angle ϕ_0. The amplitude of the emulated field can be calculated as

$$
\hat{F}_q(\phi_0) = \sum_{k=1}^{K} \exp\left(j\frac{2\pi}{\lambda}\langle \boldsymbol{r}_q, \boldsymbol{e}(\phi_k^{\mathrm{OTA}}) \rangle \right) \cdot w_k, \quad (32)
$$

where w_k is obtained through solving (13) with $\phi_{n,m} = \phi_0$ and $w_{n,m,k} = w_k$ for the single plane wave. The magnitude and the phase of $F_q(\phi_0)$ and $\hat{F}_q(\phi_0)$ for the best and the worst case are shown in Fig. 3. The white circle represents the boundary of the test area with a diameter of $1.6\,\lambda$. To tell the difference between the target and the emulated field, the RFE is used as an indicator of deviation, and is calculated as

$$
\varepsilon_q = 10 \cdot \log_{10} \frac{\left\| F_q(\phi_0) - \hat{F}_q(\phi_0) \right\|^2}{\left\| F_q(\phi_0) \right\|^2}. \quad (33)
$$

Fig. 4 shows the RFE in the region containing the test area in xy plane. The white circle indicates the boundary of the test area. Although we can see the RFE increases outside the test area in the worst case, the RFE within the test area is
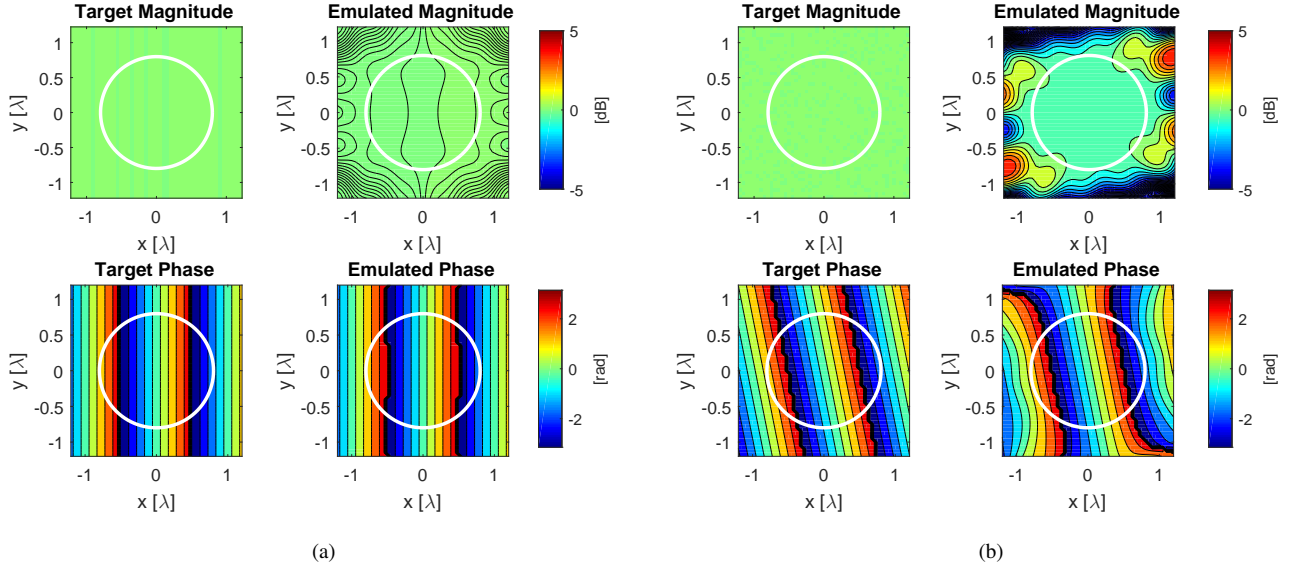
This article has been accepted for publication in a future issue of this journal, but has not been fully edited. Content may change prior to final publication. Citation information: DOI 10.1109/TVT.2018.2824403, IEEE Transactions on Vehicular Technology

7

Fig. 3. The magnitude and the phase of the target and the emulated field of a single plane wave for (a) the best case, i.e. $\phi_0 = 0°$, and (b) the worst case, i.e. $\phi_0 = 11.25°$ in the local area containing the test area. White circle denotes the boundary of the test area which is $1.6\,\lambda$ in diameter.
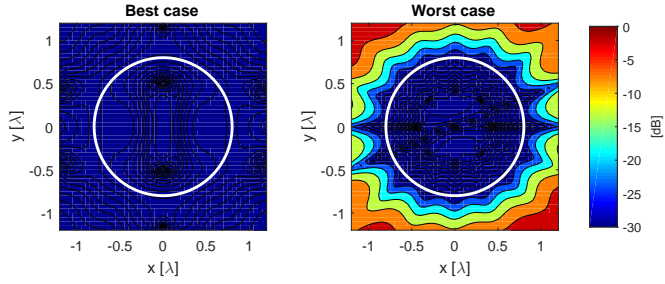

Fig. 4. RFE calculated in the local area containing the test area for (left) the best case, i.e. $\phi_0 = 0°$, and (right) the worst case, i.e. $\phi_0 = 11.25°$. White circle denotes the boundary of the test area which is $1.6\,\lambda$ in diameter.

Fig. 5. Target power spectrum in the AoA domain consisting of 20 subpaths generated according to the standards with $5°$ CASA for (top) the best case, i.e. $\bar{\phi}_0 = 0°$, and (bottom) the worst case, i.e. $\bar{\phi}_0 = 11.25°$.

always low, i.e. up to $-25\,\text{dB}$, for both cases. Therefore, the PWS method is capable of reproducing plane waves impinging from any angle with high emulation accuracy.

B. SCF on the Rx Side under Different Cluster Angular Spreads

The target channel model is changed to a single cluster with different cluster angular spreads of arrival (CASA), i.e. from $5°$ to $35°$ with $5°$ steps. The cluster is generated with its power AoA spectrum following the Laplacian distribution [1], [14]. The total power of the cluster is set to 1. In total, 20 subpaths are generated in the cluster with equal power, i.e. 0.05 each, but non-uniform AoAs as in [14, Table 4-1]. Similar to Section IV-A, the discussion is also split into the best and the worst case. The cluster mean AoA $\bar{\phi}_0$ is set to $0°$ and $11.25°$ for the best and the worst case, respectively. The target power spectrum in the AoA domain with $5°$ CASA for both cases is shown as an example in Fig. 5. A shift in the cluster mean AoA can be observed between the best case and the worst case.

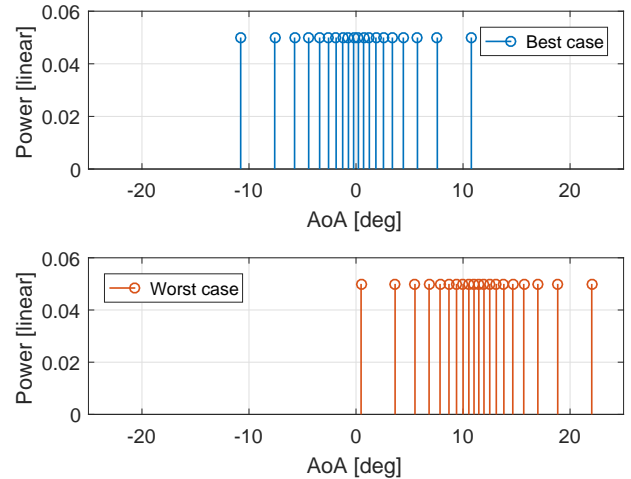The power weights for the PFS method and the complex weights for the PWS method are solved with the cost functions given in (9) and (13), respectively. The SCFs on the Rx side for the emulated channels with the PFS and the PWS method are then calculated with (22) and (28), respectively, with $s_1 = s_2$ and $t_1 = t_2$. The results are shown in Fig. 6. It can be observed that the SCF for the PWS method follows the target one almost perfectly for an antenna separation up to $1.6\,\lambda$ for all CASAs in both cases. It is because the PWS method is capable of reproducing a plane wave from arbitrary directions in the test area with a sufficient number of OTA probes as illustrated in Section IV-A.

As mentioned in the introduction, the PFS and the PWS method are usually considered to be equal in emulation
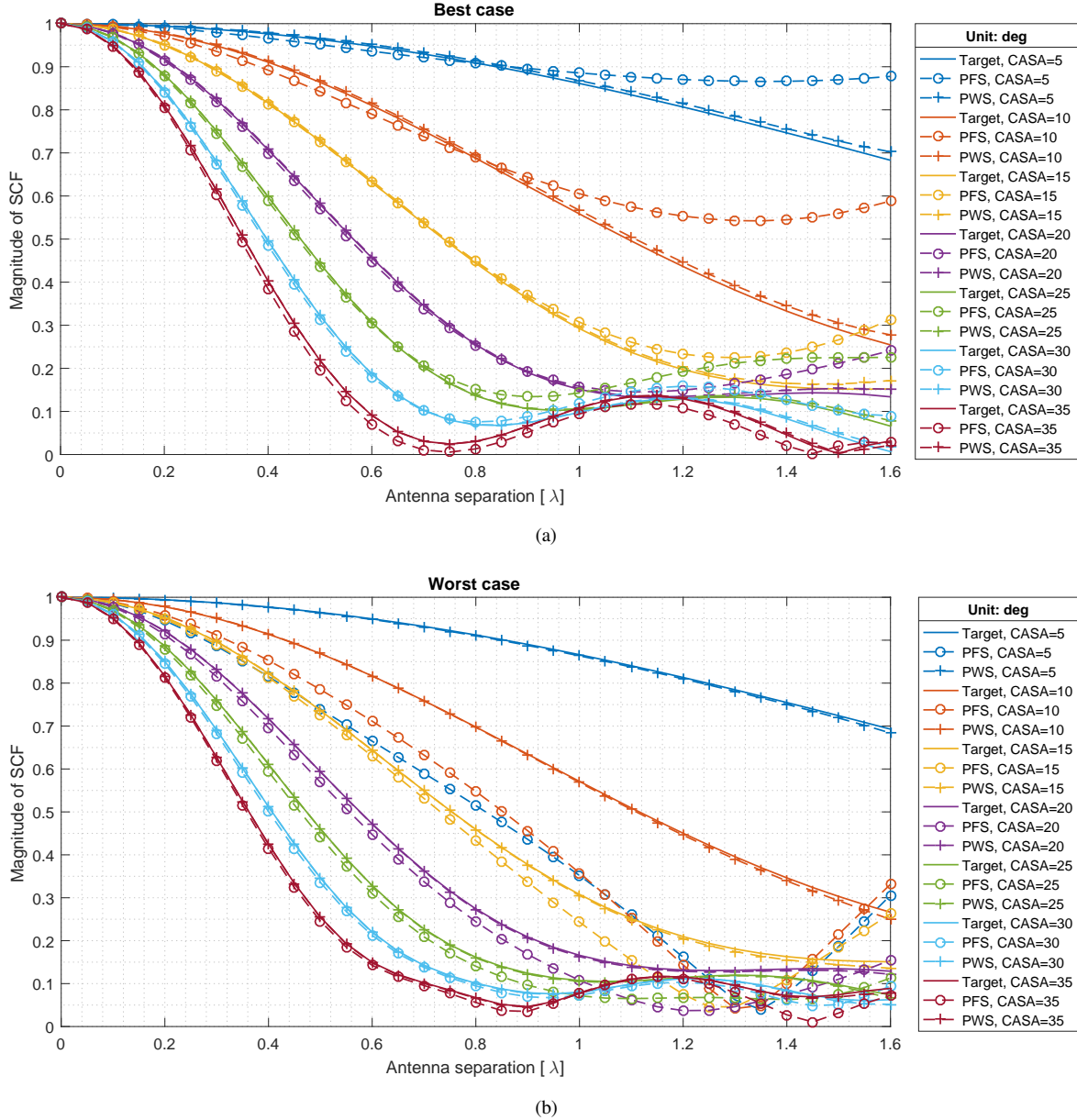
Best case
Magnitude of SCF
Antenna separation [λ]
Unit: deg
Target, CASA=5
PFS, CASA=5
PWS, CASA=5
Target, CASA=10
PFS, CASA=10
PWS, CASA=10
Target, CASA=15
PFS, CASA=15
PWS, CASA=15
Target, CASA=20
PFS, CASA=20
PWS, CASA=20
Target, CASA=25
PFS, CASA=25
PWS, CASA=25
Target, CASA=30
PFS, CASA=30
PWS, CASA=30
Target, CASA=35
PFS, CASA=35
PWS, CASA=35
Worst case
0
0.1
0.2
0.3
0.4
0.5
0.6
0.7
0.8
0.9
1
0
0.2
0.4
0.6
0.8
1
1.2
1.4
1.6

(a)

(b)

Fig. 6. The SCF on the Rx side for (a) the best case, i.e. $\bar{\phi}_0 = 0°$, and (b) the worst case, i.e. $\bar{\phi}_0 = 11.25°$, for the target and the emulated channels with the PFS and the PWS method at different CASAs, respectively.

accuracy [7], [17]. However, it can be observed in Fig. 6 the deviation in SCF for the PFS method is always larger than that for the PWS method. For both the best and the worst case, the deviation decreases with the increase of CASAs, which shows the PFS method is poor at reproducing clusters with small angular spreads. This is more obvious in the worst case as the deviation occurs at a smaller antenna separation. When the CASA is very small compared to the angular separation of adjacent OTA probes, e.g. CASA $= 5°$ and $10°$ compared to the $22.5°$ OTA probe separation, the cluster becomes very specular in angular domain. If the specular cluster comes in the direction where there is no OTA probe as in the worst case, the PFS method cannot reproduce it, and the deviation of the SCF is significant even at a small antenna separation as seen in Fig. 6(b). Recall that the supported test area size is usually determined on the largest antenna separation with respect to an acceptable deviation level in SCF. Therefore, the PWS method supports a larger test area than the PFS method with the same MPAC setup, especially at small CASAs. Note that the results presented in Fig. 6 are consistent with those reported in [7], [17], where channel models with large CASAs (i.e. $35°$) were investigated.

Nonetheless, the SCFs for both methods well follow the target at large CASAs, e.g. $30°$ and $35°$. Therefore, the emulation accuracy can be considered the same for cases such as UE testing where the CASA is large due to surrounding rich scatterers. However, for cases like BS testing where the CASA is small, e.g. $2°$ and $5°$ as for SCME Urban Micro-cell (UMi) and Urban Macro-cell (UMa) scenario respectively [13], the two methods shall not be considered the same in terms of

0018-9545 (c) 2018 IEEE. Personal use is permitted, but republication/redistribution requires IEEE permission. See http://www.ieee.org/publications_standards/publications/rights/index.html for more information.
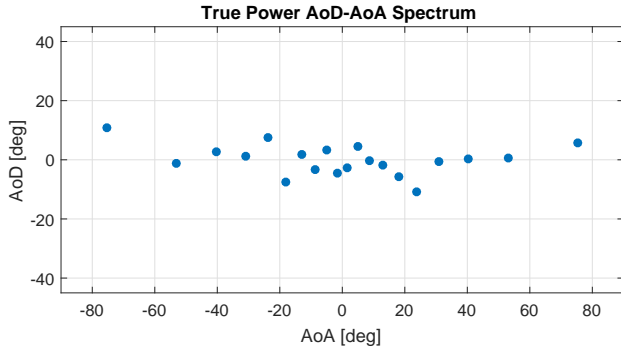
Fig. 7. True power spectrum of 20 subpaths in the joint AoD-AoA domain generated as the target channel for emulating with the PFS and the PWS method.

emulation accuracy.

C. Power Spectrum in Joint AoD-AoA Domain

The target channel is set to a single cluster. The cluster angular spread of departure (CASD) is set to $5°$, and the CASA is set to $35°$ in accordance with the SCME UMi scenario [13]. The cluster mean AoA is set to $0°$ which corresponds to the best case in Fig. 6. The cluster mean AoD is also set to $0°$. The AoD and the AoA of subpaths are randomly paired to each other. The Tx antenna array is set to a ULA of 4 isotropic antenna elements with $0.5\,\lambda$ element spacing (i.e. $1.5\,\lambda$ in array aperture). The Rx antenna array is set to a ULA with 33 isotropic antenna elements with $0.05\,\lambda$ element spacing (i.e. $1.6\,\lambda$ in array aperture). The broadsides of the Tx and the Rx array are aligned to $0°$ for the AoD and the AoA domain, respectively. This simulation setting leads to a fair comparison of the emulated channels between the PFS and the PWS method because both methods are capable of emulating the target channel in the test area of size $1.6\,\lambda$ with low errors as observed in Fig. 6. The true power AoD-AoA spectrum is shown in Fig. 7 as a reference. However, it is not observable unless we have an infinite large array aperture on both Tx and Rx side.

Alternatively, the power AoD-AoA spectrum is estimated with the Bartlett beamforming and the multiple signal classification (MUSIC) algorithm [30]. As the input for the Bartlett beamforming and the MUSIC algorithm, the joint Tx-Rx spatial correlation function is obtained from (18), (22), and (28) with $t_1 = t_2$ for the target channel, the PFS method, and the PWS method, respectively.

The estimated power AoD-AoA spectra from the Bartlett beamforming are shown in the upper row in Fig. 8. Due to the small array aperture confined in the test area, the angular resolution of the Bartlett beamforming is limited. However, we can see that the estimated power AoD-AoA spectrum for the PWS method is more consistent with that for the target channel compared to the PFS method. The MUSIC algorithm is further applied to obtain the power AoD-AoA spectra with a finer angular resolution, as shown in the lower row in Fig. 8. We can see the estimated power AoD-AoA spectrum of the target channel is more similar to the true one shown in Fig. 7. However, since the high-resolution MUSIC

algorithm is sensitive to emulation errors, the sidelobes in the power AoD-AoA spectrum for the PWS method are higher than those for the target channel. In addition, the Kronecker structure of the power AoD-AoA spectrum for the PFS method can be clearly seen from both the Bartlett beamforming and the MUSIC results, which is consistent with the correlation function analysis given in Section III-B.

Fig. 9 shows the marginal power AoD spectra and the marginal power AoA spectra obtained from the Bartlett beamforming results given in Fig. 8. It shows although the power spectra in the joint AoD-AoA domain is different between the two methods, the marginal power spectra are still the same in both domains as expected. Note the marginal power spectra of the MUSIC results are not shown due to the pseudo-spectrum of the MUSIC algorithm.

It was discussed in the literature [31], [32] that the Kronecker model usually underestimates the channel capacity, especially when the spatial correlation at either Tx side or Rx side is high. Therefore, when single cluster channel models are used during performance testing, the underlying channel capacity is supposed to be underestimated. However, for multi-cluster channel models, since the Kronecker structure only appears within the cluster, the AoDs and the AoAs are still dependent between different clusters from the whole channel point of view. In [33], [34], it was shown experimentally the difference between the target channel and the emulated channel with the PFS method is negligible in terms of capacity with small arrays, e.g. 2×2 or 4×2 MIMO. In [17], similar results were observed experimentally in terms of throughput. We postulate the difference is more pronounced for massive MIMO systems due to their higher angular resolution.

V. CONCLUSIONS

In this paper, two channel emulation methods for MIMO OTA testing with the MPAC setup, i.e. the PFS and the PWS method, are reviewed. The standard channel model, i.e. the GSCM, is used as the target channel model in this study. The signal models of the emulated channels for the two methods are given. Moreover, the STCF is derived for both methods. It shows the STCF for the PWS method is consistent with that of the target channel, whereas the STCF for the PFS method is Kronecker structured cluster-wise between the joint AoD-Doppler domain and the AoA domain. The correlation functions in the respective AoD, AoA, and Doppler domain are also derived from the STCF for both methods, which agree well with those of the target channel.

Simulation is further conducted for both methods with an MPAC setup of 16 OTA probes evenly located on the OTA ring. The SCFs on the Rx side are calculated for the target channel, the PFS method, and the PWS method at different CASAs ranging from $5°$ to $35°$ with $5°$ steps. It shows both methods are capable of reproducing clusters of large CASAs, e.g. from $20°$ to $35°$, for a test area of $1.6\,\lambda$ in size with an acceptable error. However, for a smaller CASA, only the SCF for the PWS method still maintains a good match to the target SCF. The SCF for the PFS method starts to deviate from the target SCF at a small antenna separation, especially when
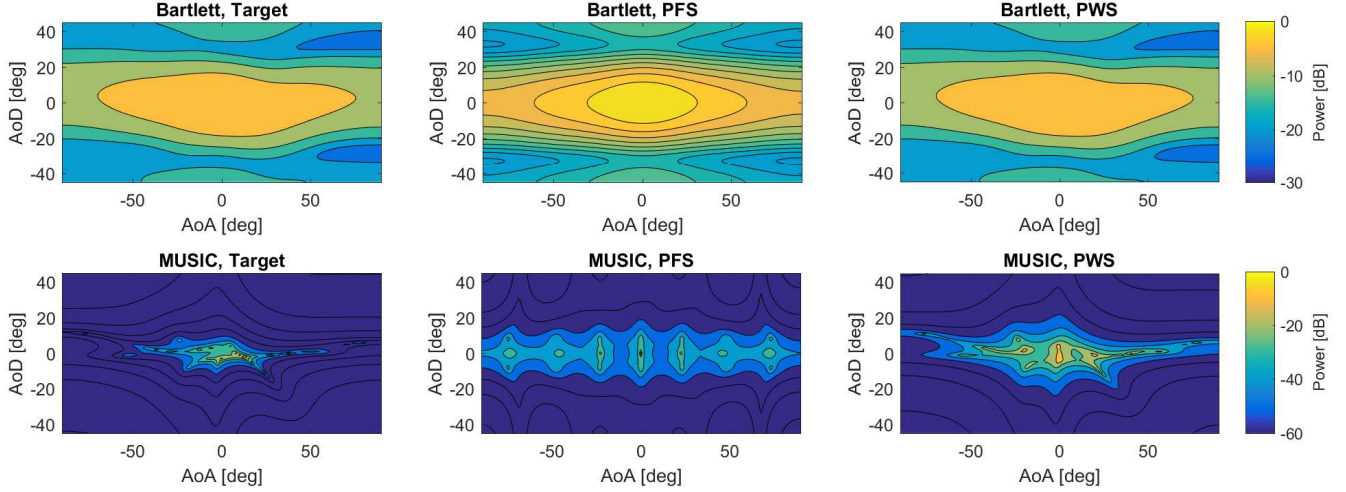
Fig. 8. The estimated power spectra in the joint AoD-AoA domain for the PFS and PWS method. The Bartlett beamforming results are shown in the upper row with $30\,\mathrm{dB}$ power range, and the MUSIC results are shown in the lower row with $60\,\mathrm{dB}$ power range.
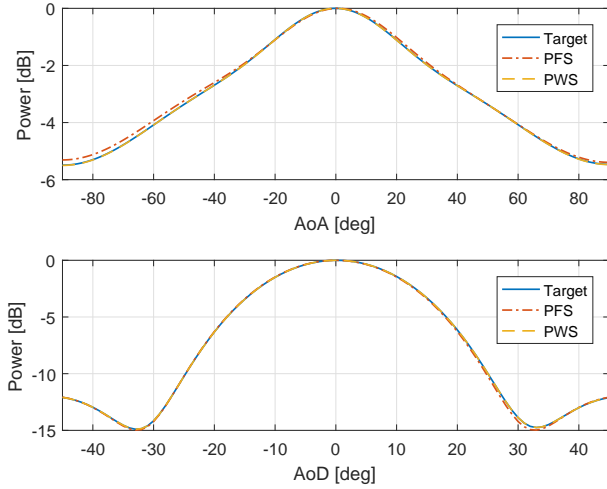

Fig. 9. The normalized marginal power spectra calculated from the Bartlett power spectrum estimated in Fig. 8 in (top) the AoA domain, and (bottom) the AoD domain.

there is no OTA probe located in the direction of the target cluster mean AoA. This difference between the PFS and the PWS method might not be observable for UE-type DUTs due to the large CASA of $35°$ according to SCME model, but it could be severe for BS-type DUTs. Therefore, it is suggested to remap the target cluster mean AoA to its closest OTA probe to achieve a better emulation accuracy for small CASAs with the PFS method.

The power spectrum in joint AoD-AoA domain is also estimated with the Bartlett beamforming and the MUSIC algorithm for the emulated channels with both methods. A good match can be seen between the estimated power spectrum for the PWS method and the target one. The Kronecker structure of the emulated cluster-wise channel with the PFS method is also observed from the estimated power spectrum. This

channel property shall be noted when the target channel model is a single cluster model for performance testing. Although this channel property did not seem to cause huge impact on UE OTA testing in terms of throughput in the literature, it might be more significant for massive MIMO systems with higher angular resolution.

Finally, the PWS method is more demanding than the PFS method in terms of calibration efforts, but in return, the emulation accuracy of the PWS method is better.

APPENDIX A
DERIVATION OF (7)

Note that $\left\|F_s^{\mathrm{Tx}}\right\| = 1$ is assumed when calculating $g_{n,k}$ to leave out the effect of Tx antenna pattern on spatial correlation. Inserting (4) into (7), we can obtain

$$
\begin{aligned}
&\rho_{\tilde{u}_1, \tilde{u}_2} \\
&= \frac{1}{\beta_0} \cdot \mathrm{E}\left\{ h_{\tilde{u}_1,s,n}(t,f) \cdot h_{\tilde{u}_2,s,n}(t,f)^* \right\} \\
&= \frac{1}{\beta_0} \frac{P_n}{M} \cdot \mathrm{E}\Bigg\{ \Bigg[\sum_{m=1}^{M} F_s^{\mathrm{Tx}}(\varphi_{n,m}) F_{\tilde{u}_1}^{\mathrm{VA}}(\phi_{n,m}) \\
&\quad \cdot \exp(j2\pi\vartheta_{n,m}t + j\Phi_{n,m}) \cdot \exp(-j2\pi f\tau_n) \Bigg] \\
&\quad \cdot \Bigg[\sum_{m'=1}^{M} F_s^{\mathrm{Tx}}(\varphi_{n,m'}) F_{\tilde{u}_2}^{\mathrm{VA}}(\phi_{n,m'}) \\
&\quad \cdot \exp(j2\pi\vartheta_{n,m'}t + j\Phi_{n,m'}) \cdot \exp(-j2\pi f\tau_n) \Bigg]^* \Bigg\}, \quad (34)
\end{aligned}
$$

where $\beta_0 = P_n$ is the normalization factor. Since we have

$$
\begin{aligned}
&\mathrm{E}\left\{ \exp(j\Phi_{n,m}) \exp(j\Phi_{n,m'})^* \right\} \\
&= \begin{cases} 1 & \text{when } m = m' \\ 0 & \text{when } m \neq m' \end{cases}, \quad (35)
\end{aligned}
$$

(34) can be simplified to

$$\rho_{\tilde{u}_1,\tilde{u}_2} = \frac{1}{M} \sum_{m=1}^{M} F_{\tilde{u}_1}^{\mathrm{VA}}(\phi_{n,m}) F_{\tilde{u}_2}^{\mathrm{VA}}(\phi_{n,m})^*, \qquad (36)$$

by taking only the terms with $m = m'$ into account.

APPENDIX B
DERIVATION OF (8)

As mentioned in Appendix A, $\left\|F_s^{\mathrm{Tx}}\right\| = 1$ is assumed when calculating $g_{n,k}$ to leave out the effect of Tx antenna pattern on spatial correlation. Inserting (6) into (8), we can obtain

$$\hat{\rho}_{\tilde{u}_1,\tilde{u}_2}$$
$$= \frac{1}{\hat{\beta}_0} \cdot \mathrm{E}\left\{ \hat{h}_{\tilde{u}_1,s,n}^{\mathrm{PFS}}(t,f) \cdot \hat{h}_{\tilde{u}_2,s,n}^{\mathrm{PFS}}(t,f)^* \right\}$$
$$= \frac{1}{\hat{\beta}_0} \frac{P_n}{M} \cdot \mathrm{E}\left\{ \left[\sum_{k=1}^{K} \sum_{m=1}^{M} F_s^{\mathrm{Tx}}(\varphi_{n,m}) F_{\tilde{u}_1}^{\mathrm{VA}}(\phi_k^{\mathrm{OTA}}) \sqrt{g_{n,k}} \right. \right.$$
$$\left. \cdot \exp(j2\pi\vartheta_{n,m}t + j\Phi_{n,m,k}) \cdot \exp(-j2\pi f\tau_n) \right]$$
$$\cdot \left[\sum_{k'=1}^{K} \sum_{m'=1}^{M} F_s^{\mathrm{Tx}}(\varphi_{n,m'}) F_{\tilde{u}_2}^{\mathrm{VA}}(\phi_{k'}^{\mathrm{OTA}}) \sqrt{g_{n,k'}} \right.$$
$$\left. \left. \cdot \exp(j2\pi\vartheta_{n,m'}t + j\Phi_{n,m',k'}) \cdot \exp(-j2\pi f\tau_n) \right]^* \right\}, \quad (37)$$

where $\hat{\beta}_0 = P_n$ is the normalization factor. Regarding

$$\mathrm{E}\left\{ \exp(j\Phi_{n,m,k}) \exp(j\Phi_{n,m',k'})^* \right\}$$
$$= \begin{cases} 1 & \text{when } m = m' \text{ and } k = k' \\ 0 & \text{when } m \neq m' \text{ or } k \neq k' \end{cases}, \qquad (38)$$

(37) can be simplified to

$$\hat{\rho}_{\tilde{u}_1,\tilde{u}_2} = \sum_{k=1}^{K} g_{n,k} F_{\tilde{u}_1}^{\mathrm{VA}}(\phi_k^{\mathrm{OTA}}) F_{\tilde{u}_2}^{\mathrm{VA}}(\phi_k^{\mathrm{OTA}})^*, \qquad (39)$$

by taking only the terms with $m = m'$ and $k = k'$ into account.

ACKNOWLEDGMENT

REFERENCES

[1] 3GPP, "Measurement of radiated performance for Multiple Input Multiple Output (MIMO) and multi-antenna reception for High Speed Packet Access (HSPA) and LTE terminals," Technical Specification Group Radio Access Network, Tech. Rep. 3GPP TR 37.976 V11.0.0, 2012.

[2] W. Yu, Y. Qi, S. Member, K. Liu, Y. Xu, and A. Two-stage, "Radiated Two-Stage Method for LTE MIMO User," *IEEE Transactions on Electromagnetic Compatibility*, vol. 56, no. 6, pp. 1691–1696, 2014.

[3] W. Fan, P. Kyösti, L. Hentilä, and G. F. Pedersen, "MIMO Terminal Performance Evaluation With a Novel Wireless Cable Method," *IEEE Transactions on Antennas and Propagation*, vol. 65, no. 9, pp. 4803–4814, 2017.

[4] P. S. Kildal and K. Rosengren, "Correlation and capacity of MIMO systems and mutual coupling, radiation efficiency, and diversity gain of their antennas: Simulations and measurements in a reverberation chamber," *IEEE Communications Magazine*, vol. 42, no. 12, pp. 104–112, 2004.

[5] X. Chen, "Throughput modeling and measurement in an isotropic-scattering reverberation chamber," *IEEE Transactions on Antennas and Propagation*, vol. 62, no. 4, pp. 2130–2139, 2014.

[6] J. T. Toivanen, T. A. Laitinen, V. M. Kolmonen, and P. Vainikainen, "Reproduction of arbitrary multipath environments in laboratory conditions," *IEEE Transactions on Instrumentation and Measurement*, vol. 60, no. 1, pp. 275–281, 2011.

[7] P. Kyösti, T. Jämsä, and J.-P. Nuutinen, "Channel modelling for multiprobe over-the-air MIMO testing," *International Journal of Antennas and Propagation*, vol. 2012, 2012.

[8] R. K. Sharma, W. Kotterman, M. H. Landmann, C. Schirmer, C. Schneider, F. Wollenschläger, G. Del Galdo, M. A. Hein, and R. S. Thomä, "Over-the-Air Testing of Cognitive Radio Nodes in a Virtual Electromagnetic Environment," *International Journal of Antennas and Propagation*, vol. 2013, 2013.

[9] A. Khatun, V. M. Kolmonen, V. Hovinen, D. Parveg, M. Berg, K. Haneda, K. I. Nikoskinen, and E. T. Salonen, "Experimental Verification of a Plane-Wave Field Synthesis Technique for MIMO OTA Antenna Testing," *IEEE Transactions on Antennas and Propagation*, vol. 64, no. 7, pp. 3141–3150, 2016.

[10] Y. Jing, X. Zhao, H. Kong, S. Duffy, and M. Rumney, "Two-Stage Over-the-Air (OTA) TEST METHOD for LTE MIMO Device Performance Evaluation," *International Journal of Antennas and Propagation*, vol. 2012, 2012.

[11] CTIA, "Test Plan for 2x2 Downlink MIMO and Transmit Diversity Over-the-Air Performance," Tech. Rep. Version 1.1.1, 2017.

[12] 3GPP, "Spatial channel model for Multiple Input Multiple Output (MIMO) simulations," Tech. Rep. 3GPP TR 25.996 V12.0.0, 2014.

[13] D. S. Baum, J. Hansen, G. D. Galdo, and M. Milojevic, "An Interim Channel Model for Beyond-3G Systems," *Vehicular Technology Conference, 2005. VTC 2005-Spring. 2005 IEEE 61st*, vol. 5, pp. 3132–3136, 2005.

[14] WINNER, "WINNER II Channel Models: Part I Channel Models," Tech. Rep. D1.1.2 V1.2, 2007.

[15] W. Fan, X. Carreño, F. Sun, J. Ø. Nielsen, M. B. Knudsen, and G. F. Pedersen, "Emulating spatial characteristics of MIMO channels for OTA testing," *IEEE Transactions on Antennas and Propagation*, vol. 61, no. 8, pp. 4306–4314, 2013.

[16] W. Fan, P. Kyösti, J.-P. Nuutinen, À. O. Martínez, J. Ø. Nielsen, and G. F. Pedersen, "Generating spatial channel models in multi-probe anechoic chamber setups," in *Vehicular Technology Conference (VTC Spring), 2016 IEEE 83rd*, 2016, pp. 1–5.

[17] M. S. Miah, D. Anin, A. Khatun, K. Haneda, L. Hentilä, and E. T. Salonen, "On the Field Emulation Techniques in Over-the-air Testing: Experimental Throughput Comparison," *IEEE Antennas and Wireless Propagation Letters*, vol. 16, pp. 2224–2227, 2017.

[18] P. Bello, "Characterization of Randomly Time-Variant Linear Channels," *IEEE Transactions on Communications Systems*, vol. 11, no. 4, pp. 360–393, 1963.

[19] B. H. Fleury, "First- and second-order characterization of direction dispersion and space selectivity in the radio channel," *IEEE Transactions on Information Theory*, vol. 46, no. 6, pp. 2027–2044, 2000.

[20] R. Vaughan and J. B. Andersen, *Channels , Propagation and Antennas for Mobile Communications*. The Institution of Electrical Engineers, 2003.

[21] R. He, B. Ai, G. L. Stuber, G. Wang, and D. Z. Zhong, "Geometrical Based Modeling for Millimeter Wave MIMO Mobile-to-Mobile Channels," *IEEE Transactions on Vehicular Technology*, vol. PP, no. 99, pp. 1–16, 2017.

[22] J. Meinilä, P. Kyösti, L. Hentilä, T. Jämsä, E. Suikkanen, E. Kunnari, and M. Narandžić, "D5.3: WINNER+ Final Channel Models," Tech. Rep., 2010.

[23] S. Boyd and L. Vandenberghe, *Convex Optimization*. Cambridge University Press, 2004.

[24] W. Fan, X. Carreño, J. Ø. Nielsen, K. Olesen, M. B. Knudsen, and G. F. Pedersen, "Measurement verification of plane wave synthesis technique based on multi-probe MIMO-OTA setup," in *IEEE Vehicular Technology Conference (VTC Fall)*, 2012, pp. 1–5.

[25] E. G. Larsson, O. Edfors, F. Tufvesson, and T. L. Marzetta, "Massive MIMO for next generation wireless systems," *IEEE Communications Magazine*, vol. 52, no. 2, pp. 186–195, 2014.

This article has been accepted for publication in a future issue of this journal, but has not been fully edited. Content may change prior to final publication. Citation information: DOI 10.1109/TVT.2018.2824403, IEEE Transactions on Vehicular Technology

12

[26] K. Guan, G. Li, T. Kurner, A. F. Molisch, B. Peng, R. He, B. Hui, J. Kim, and Z. Zhong, "On Millimeter Wave and THz Mobile Radio Channel for Smart Rail Mobility," *IEEE Transactions on Vehicular Technology*, vol. 66, no. 7, pp. 5658–5674, 2017.

[27] B. Ai, K. Guan, R. He, J. Li, G. Li, D. He, Z. Zhong, and K. M. S. Huq, "On Indoor Millimeter Wave Massive MIMO Channels: Measurement and Simulation," *IEEE Journal on Selected Areas in Communications*, vol. 35, no. 7, pp. 1678–1690, 2017.

[28] P. Kyösti, W. Fan, and J. Kyröläinen, "Assessing measurement distances for OTA testing of massive MIMO base station at 28 GHz," in *2017 11th European Conference on Antennas and Propagation, EUCAP 2017*, 2017, pp. 3679–3683.

[29] C. Oestges, "Validity of the Kronecker Model for MIMO Correlated Channels," in *Vehicular Technology Conference, 2006. VTC 2006-Spring. IEEE 63rd*, vol. 6, 2006, pp. 2818–2822.

[30] H. Krim and M. Viberg, "Two decades of array signal processing research: The parametric approach," *IEEE Signal Processing Magazine*, vol. 13, no. 4, pp. 67–94, 1996.

[31] H. Özcelik, M. Herdin, W. Weichselberger, J. Wallace, and E. Bonek, "Deficiencies of 'Kronecker' MlMO radio channel model," *Electronics Letters*, vol. 39, no. 16, pp. 1209–1210, 2003.

[32] V. Raghavan, J. H. Kotecha, and A. M. Sayeed, "Why does the Kronecker model result in misleading capacity estimates?" *IEEE Transactions on Information Theory*, vol. 56, no. 10, pp. 4843–4864, 2010.

[33] W. Fan, P. Kyösti, J. Ø. Nielsen, and G. F. Pedersen, "Wideband MIMO Channel Capacity Analysis in Multiprobe Anechoic Chamber Setups," *IEEE Transactions on Vehicular Technology*, vol. 65, no. 5, pp. 2861–2871, 2016.

[34] W. Fan, L. Hentilä, P. Kyösti, and G. F. Pedersen, "Test Zone Size Characterization with Measured MIMO Throughput for Simulated MPAC Configurations in Conductive Setups," *IEEE Transactions on Vehicular Technology*, vol. 66, no. 11, pp. 10 532–10 536, 2017.
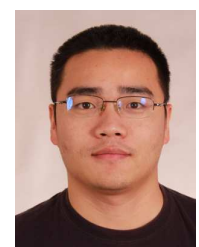
Gert Frølund Pedersen was born in 1965 and married to Henriette and have 7 children. He received the B.Sc. E.E. degree, with honour, in electrical engineering from College of Technology in Dublin, Ireland in 1991, and the M.Sc. E.E. degree and Ph.D. from Aalborg University in 1993 and 2003. He has been with Aalborg University since 1993 where he is a full Professor heading the Antenna, Propagation and Networking LAB with 36 researcher. Further he is also the head of the doctoral school on wireless communication with some 100 phd students enrolled. His research has focused on radio communication for mobile terminals especially small Antennas, Diversity systems, Propagation and Biological effects and he has published more than 175 peer reviewed papers and holds 28 patents. He has also worked as consultant for developments of more than 100 antennas for mobile terminals including the first internal antenna for mobile phones in 1994 with lowest SAR, first internal triple-band antenna in 1998 with low SAR and high TRP and TIS, and lately various multi-antenna systems rated as the most efficient on the market. He has worked most of the time with joint university and industry projects and have received more than 12 M$ in direct research funding. Latest he is the project leader of the SAFE project with a total budget of 8 M$ investigating tunable front end including tunable antennas for the future multiband mobile phones. He has been one of the pioneers in establishing Over-The-Air (OTA) measurement systems. The measurement technique is now well established for mobile terminals with single antennas and he was chairing the various COST groups (swg2.2 of COST 259, 273, 2100 and now ICT1004) with liaison to 3GPP for over-the-air test of MIMO terminals. Presently he is deeply involved in MIMO OTA measurement.
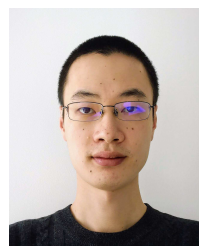
Yilin Ji received his B.Sc. degree in Electronics Science and Technology and M.Eng degree in Integrated Circuit Engineering from Tongji University, China, in 2013 and 2016, respectively. He is currently a Ph.D. fellow at the Antennas, Propagation and Millimeter-wave Systems (APMS) section at Aalborg University, Denmark. His main research areas are propagation channel characterization, indoor localization, and MIMO over-the-air testing.

Xingfeng Wu received his Master and Ph.D. degree from Beijing University of Posts and Telecommunications in 2003 and 2007, respectively. From July 2007 to June 2016, he was the director of EMC and OTA Lab in wireless research department with Academy of Broadcasting Planning China. From December 2011 to December 2012, he stayed in University of York, UK as a visiting scholar. He is currently working on the OTA method for 5G mmWave measurement at Huawei technology as the chief testing engineer in Consumer Business Group in Beijing. His interests of research are over-the-air testing, channel and propagation.

Wei Fan received his Bachelor of Engineering degree from Harbin Institute of technology, China in 2009, Masters double degree with highest honours from Politecnico di Torino, Italy and Grenoble Institute of Technology, France in 2011, and Ph.D. degree from Aalborg University, Denmark in 2014. From February 2011 to August 2011, he was with Intel Mobile Communications, Denmark as a research intern. He conducted a three-month internship at Anite telecoms oy, Finland in 2014. His main areas of research are over the air testing of multiple antenna systems, radio channel sounding, modelling and emulation. He is currently an associate professor at the Antennas, Propagation and Millimeterwave Systems (APMS) Section at Aalborg University.